







Generation of shock trains in free liquid jets with a nanosecond green laser

Daniel Ursescu ¹, Veselin Aleksandrov ¹, Dan Matei ¹, Ioan Dancus ¹,
Matias D. de Almeida ² and Claudiu A. Stan ^{2,*}

¹*Extreme Light Infrastructure-Nuclear Physics (ELI-NP), Horia Hulubei National R&D Institute for Physics and Nuclear Engineering (IFIN-HH), 077125 Măgurele, Romania*

²*Department of Physics, Rutgers University Newark, Newark, New Jersey 07102, USA*



(Received 14 July 2020; accepted 9 November 2020; published 8 December 2020)

Shock wave trains in liquid jets were previously generated only by ablation with femtosecond x-ray lasers. Here we show that shock trains in water microjets can be also generated using nanosecond green laser pulses with 1- to 10-mJ energy. The ablation of 15-, 20-, 30-, and 70- μm water microjets opened a gap in the jets and launched an initial shock wave. Fully developed shock trains were observed in the 30- and 70- μm jets up to 250-ns delays, and these trains were also transmitted inside the nozzles. A few tens of nanoseconds after the pulse, the shock dynamics and its pressure became similar to the ones generated by x-ray lasers, with a more rapid pressure decay in thinner jets. At time delays exceeding 100 ns in the 30- μm jets, the leading shock pressure stabilized to an approximately constant pressure of 40 MPa. The energy density deposited in the jets was estimated at 30 MJ/cm³ by comparing the jet gaps in the green and x-ray laser experiments, and matched previous estimates for optical ablation in water. The pressure decay in the 30- μm jets was modeled based on the pressure decay observed in x-ray laser experiments.

DOI: [10.1103/PhysRevFluids.5.123402](https://doi.org/10.1103/PhysRevFluids.5.123402)

I. INTRODUCTION

Laser ablation in microscale liquid systems has practical applications in which understanding the hydrodynamics driven by ablation is critical, such as producing extreme ultraviolet light for the semiconductor industry [1–3] and developing biological imaging experiments at x-ray free-electron laser (XFEL) facilities [4]. The fluid dynamics driven by ablation also has basic research applications, such as inducing cavitation at large negative pressures [5–7] and generating microscale focused shock waves [8].

As new types of light sources become available, the hydrodynamics of ablation is likely to find new applications and expose new phenomena. For example, there is a growing interest [9,10] in using liquid targets at state-of-the-art optical laser facilities designed to generate unprecedented light intensities [11]. Given that such light pulses will destroy the samples, liquid targets are advantageous because they can be replenished rapidly, thus taking full advantage of the high pulse repetition rates (>1 Hz) available at the newest facilities [12]. While the initial designs of targets for petawatt lasers will benefit from the extensive development of liquid targets at x-ray laser facilities [13–15], the physical mechanisms of liquid ablation with petawatt optical lasers are yet to be investigated. These mechanisms could influence the design of the liquid targets and lead to new applications.

Recent studies of ablation in liquids using x-ray lasers expanded the understanding of ablation hydrodynamics and suggested new research directions. Ablation with pulsed x-ray lasers of microjets [4,16] and microdrops [6,17] differs from ablation with optical lasers because the energy

*claudiu.stan@rutgers.edu

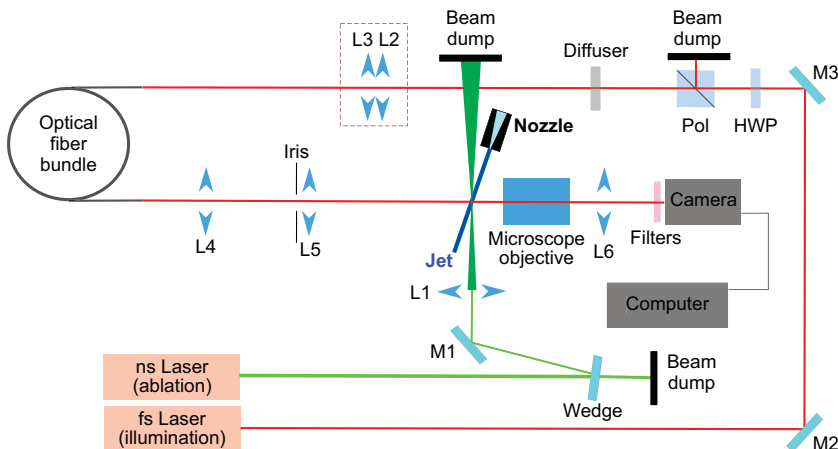


FIG. 1. Experimental setup. Water microjets were ablated with a nanosecond laser and imaged using a femtosecond laser. M1, M2, and M3: silver mirrors; L1 ($f = 25$ mm), L2 ($f = 100$ mm), L3 ($f = 125$ mm), L4 ($f = 75.6$ mm), L5 ($f = 38.1$ mm), and L6 ($f = 125$ mm): lenses; HWP: half waveplate; Pol: polarizing beamsplitter cube.

absorption of x rays is linear and predictable and can be concentrated in a smaller region. These characteristics lead to a relatively simpler hydrodynamics that is more amenable to analytical and numerical modeling [4,18,19] and allow studies at smaller length and timescales, which are advantageous for generating metastable states such as negative pressures [6]. Ablation with x-ray lasers also led to the observation of new hydrodynamic phenomenon: the generation of shock wave trains in liquid water jets [4]. These shock trains represent the most intense sound waves measured to date in liquid water [16], with an estimated sound pressure level above 270 dB (re: $1 \mu\text{Pa}$).

Liquid ablation with x-ray lasers is a useful tool to study shock waves, cavitation, and extremely high intensity sound, but the capacity of x-ray laser facilities to conduct such experiments is very limited. Fortunately, laboratory-scale optical lasers can replicate some of the x-ray laser ablation phenomena, in particular those involving microjets. For example, the formation of ablation gaps in jets was first observed using optical lasers [20]. It was also predicted that shock trains in liquid jets can be generated using optical lasers [16].

Here we report that shock wave trains can be generated in water microjets using a nanosecond green laser (532 nm) with pulse energies ranging from approximately 1 to 10 mJ. We also found that in sufficiently large diameter jets the shock trains can travel distances much larger than the jet diameter while maintaining peak pressures of tens of megapascals and can be transmitted inside the nozzles that produced the jets.

II. EXPERIMENTAL DESIGN

The experiments were conducted in the Optics Laboratory [21] at the Extreme Light Infrastructure-Nuclear Physics (ELI-NP) facility in Măgurele, Romania [12]. A schematic of the setup is shown in Fig. 1. Downward-flowing liquid water microjets with diameters of 15, 20, 30, and $70 \mu\text{m}$ were produced at ambient conditions (atmospheric pressure, 22°C) by tapered glass nozzles (MJ-AT series, MicroFab Inc., Plano, TX).

The jets were subjected to focused nanosecond green laser pulses (Thales SAGA, 5 ns, 532 nm, 1.8 J, 10 Hz) propagating horizontally, perpendicular to the jet axis. The laser pulses were attenuated to pulse energies ranging from 1 to 10 mJ. The laser beam had a diameter of 11 mm and was focused onto the jet using a best-form aspheric lens with a 25-mm focal length (Edmund Optics). The characteristics of the laser pulses were chosen to (i) exceed the intensity threshold at which

optical breakdown in liquid water was previously observed [22] and (ii) achieve a focused beam size smaller than the jet diameter, because previous data from x-ray lasers suggests that the generation of shock trains requires a beam size smaller than the jet diameter [16,23]. Based on the focusing optics and on the laser beam quality factor ($M^2 \approx 2.5$) the beam focus size will be $4 \mu\text{m}$, less than the $15\text{-}\mu\text{m}$ diameter of the thinnest jet used. However, the laser had a multimode beam with at least two distinct high intensity peaks (hot spots) in the focal plane.

The ablation was imaged using a horizontal microscope setup with $10\times$ and $20\times$ objectives, in a pump-probe mode, with single images recorded after each ablation pulse at variable time delays ranging from 0 to ≈ 800 ns. The imaging axis was perpendicular to both the jet and the ablation beam, and femtosecond light pulses (Avesta Ltd., 60 fs, 800 nm) were used for illumination to avoid motion blurring when imaging shocks at a length scale of few microns. The images were recorded by a camera (Basler AG, acA2440-20gm) fitted with two narrow-bandpass filters that transmitted $\approx 50\%$ of the 800 nm imaging light but attenuated any 532-nm ablation light by a factor of $\approx 10^{11}$ (Thorlabs).

To record data, the average pulse energies were measured before the focusing lens for four distinct laser settings corresponding to energies of approximately 1, 3, 6, and 10 mJ. For a given jet diameter and laser pulse energy, approximately 70 images of the ablated jets were recorded at each time delay, to average the variations in the pulse energies and time delays. The root mean square (rms) jitter of the pulse energies ranged from 5% at 1 mJ to 2% at 10 mJ. We estimated that the time delays between the ablation pulse and the imaging flash had a rms jitter of ≈ 1 ns, based on the probability of observing the same stage of ablation in two data sets recorded at time delays differing by 3 or 5 ns.

III. RESULTS

A. Generation of shock wave trains by 532-nm laser pulses

During XFEL-induced jet ablation [4,16], the x-ray beam deposits energy into a filament of liquid thinner than the jet, leading to the formation of a plasma with high energy density and high pressure, on a picosecond timescale. The plasma then launches a shock wave into the surrounding liquid and expands rapidly against the jet. The plasma expansion generates a gap in the jet by pushing liquid from the jet into thin liquid films. Meanwhile, the initial shock starts to travel inside the jet, continuously reflecting at the jet surface. The shock interferes destructively with its reflection [24], which leads to a decrease of its pressure and to the generation of secondary shocks that travel along with jet, as a train of shocks with an intershock spacing on the order of the jet diameter.

Here we probed the jet ablation and the generation of shocks at 10–15 different time delays up to ≈ 800 ns. This is an approximately two orders of magnitude coarser temporal sampling than in the XFEL studies, but it was sufficient to confirm that similar, though not identical, phenomena occur. Same as in XFEL studies, we observed the formation and growth of a gap in the jet, as well as the generation of an initial shock that evolved into a shock train traveling inside the jet. These processes are illustrated in Fig. 2 using images of the jets, and further images are available as Supplemental Materials [25].

Figure 2 also illustrates several differences from XFEL experiments. Since our experiment was conducted not in vacuum but at ambient conditions, optical breakdown occurred both in the liquid jets with a $\approx 1\text{-mJ}$ threshold, and in air with a $\approx 3\text{-mJ}$ threshold. At pulse energies above $\approx 3\text{-mJ}$ the ablation of the liquid jet was accompanied by the formation of a breakdown plasma in air, and the dynamics of the plasma generated by the air breakdown (the “air plasma”) is shown in Figs. 2(a1)–2(a4) for 5.5-mJ pulses and a $15\text{-}\mu\text{m}$ -diameter jet. The air plasma was initially opaque and appeared dark up to time delays of 10–20 ns. The air plasma drove a shock wave in air, whose boundary can be observed in Fig. 2(a3). The center of the air plasma was located along the ablation beam, after the jet. As the air plasma expanded, it impinged upon the jets, generating wrinkles on their surface and bending them in a direction opposite to the propagation of the laser pulse.

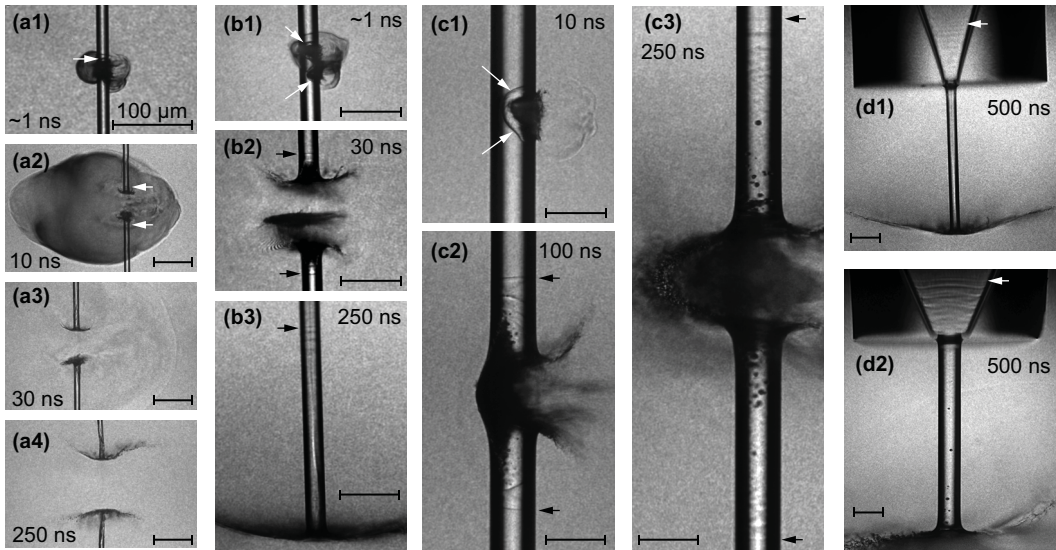


FIG. 2. Water microjets with 15- to 70- μm diameters after ablation by a focused laser pulse in air. The jets flowed downstream and the laser pulse propagated horizontally from right to left. The time delays written in the images represent the time elapsed from the laser pulse. The white or black arrows indicate the location of the leading shock waves. Panels (d1) and (d2) show shock waves transmitted inside the glass nozzles that produced the jets. The dimension bar is 100 μm in all images.

The effect of the air plasma depended on the mass of the jet, with the wrinkling and the bending being severe in the 15- and 20- μm diameter jets [see Fig. 2(a4)] but almost not observable in the 70- μm -diameter jets.

The images of the 15- μm jet illustrate the formation of the gap and of the liquid films at the jet ends. In 15- and 20- μm jets the gap was roughly symmetric to the jet axis, same as in liquid jet ablation with either x-ray or optical lasers [4,10,20,26]. In the 30- and 70- μm jets the initial growth of the gap was asymmetric and concentrated on the side facing the ablation pulse.

Ablation images for a 30- μm jet and 3.2-mJ pulses are shown in Figs. 2(b1)–2(b3), and images for a 70- μm jet and 1.1-mJ pulses are shown in Figs. 2(c1)–2(c3). Shortly after the pulse arrival [see Figs. 2(b1) and 2(c1)], dark regions inside the jet indicate regions where optical breakdown occurred in the liquid and an opaque plasma (the “water plasma”) formed. Due to the strong nonlinear absorption of the 532-nm laser pulse, the plasma formed on the side facing the incoming pulse and did not extend fully across the jet. The thin dark lines outside the water plasma are shock waves generated by the high pressure in the plasma.

The multimode pattern of the focused beam was visible in the 30- and 70- μm jets. In Fig. 2(b1), two distinct water plasma regions or lobes can be seen, illustrating the presence of two high-intensity regions (“hot spots”) vertically separated by $\approx 40 \mu\text{m}$. In Fig. 2(c1) the plasma has modulations compatible with two hot spots $\approx 35 \mu\text{m}$ apart. In the 30- μm jet, the two hot spots generated a gap that included nonvaporized liquid [see Fig. 2(b2)], therefore this gap can be interpreted as consisting of two smaller gaps, each generated by one of the hot spots.

Different from the XFEL experiments, the initial shock was not perpendicular to the jet axis in the 30- and 70- μm -diameter jets. Nevertheless, shock trains perpendicular to the jet formed and traveled for long distances. These shocks could be seen inside the nozzles as well, as shown in Figs. 2(d1) and 2(d2). In the 30- μm jet, up to four shock fronts perpendicular to the jet axis were observed, and the separation and parallelism of the shocks in the jet were preserved inside the nozzle. In the 70- μm jet, three shocks perpendicular to the jet axis were followed by weaker oblique wave fronts

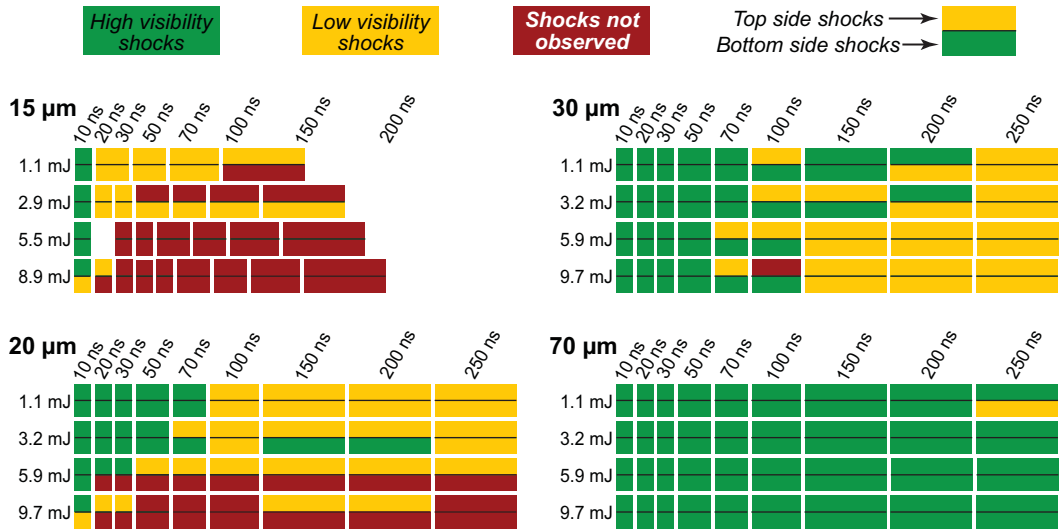


FIG. 3. The visibility of shock waves for different time delays, jet diameters, and pulse energies. Shocks were more visible in wider jets and when driven by lower energy pulses.

[see Fig. 2(c3)]. The corresponding pattern of shocks inside the nozzle [Fig. 2(d2)] preserved both the perpendicular and the oblique wave fronts.

The transition from a curved initial shock [see Fig. 2(b1) and 2(c1)] to a leading shock perpendicular to the jet [see Figs. 2(b3) and 2(c3)] is the phenomenon that explains the similarity of shock trains generated by XFELs and by green laser pulses. After a leading shock perpendicular to the jet is formed, its evolution—including generating shock trains—will depend on the shock amplitude and the jet diameter but not on how it was generated. Qualitatively, the transition to a perpendicular shock front can be explained by the nonlinear interaction of the shock with the jet surface, which generates reflected waves that catch up with the shock and interfere destructively with it, lowering its pressure and thus its propagation velocity. For shocks that are not perpendicular to the jet, the part of the shock front that is most advanced along the jet axis will be caught up first by reflections and will slow down most rapidly, until the shock assumes a front equally advanced along the jet axis (i.e., perpendicular to it.)

Shock waves were always observed at 10 ns, but their existence at longer time delays depended on both the jet diameter and the pulse energy. The existence of shock trains is summarized in Fig. 3. We characterized the recorded images as (i) having high shock visibility if the leading shock in the train was visible in all recorded images, (ii) having low shock visibility if the shocks could be discerned in only part of the recorded images, and (iii) not displaying any discernible shocks. At a given set of conditions, the shock visibility was often different for the top and the bottom shocks, because the jets had a small angle to the vertical direction and were not perfectly in focus across the whole image.

Overall, Fig. 3 illustrates that (i) the shock trains traveled for longer distances as the jet diameter increased, and that (ii) the shock trains traveled for shorter distances as the pulse energy became larger. Both trends are consistent with the prediction that efficient generation of shock trains requires that the size of the region where the energy is deposited by the beam (i.e., the water plasma) is smaller than the jet diameter [16]. As the jet diameter increases, the size of the plasma region becomes smaller relative to the jet diameter. As the pulse energy increases, the volume of high-irradiance region where plasma is generated increases, both in absolute value and relative to the jet size.

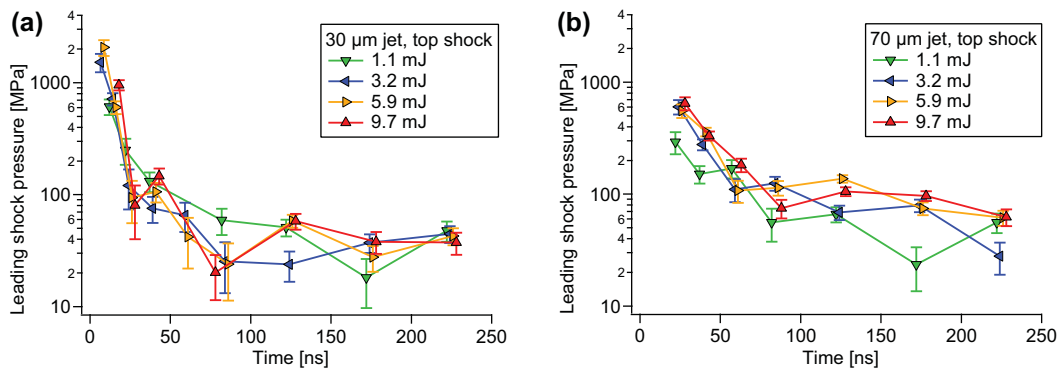


FIG. 4. The pressure of the leading shock wave and its decay in (a) 30- μm jets and (b) 70- μm jets, for the pulse energies shown in the legend. To help distinguish data sets for different pulse energies, the data are plotted shifted by -3 , -1 , 1 , and 3 ns at 1.1, 3.2, 5.7, and 9.7 mJ, respectively.

The rapid loss of the shock visibility in the thinner jets can be explained by the fact that the shock trains are more rapidly attenuated in thinner jets [16], and by two additional phenomena. First, the shock waves are less visible at the same pressure amplitude in smaller jets, because they deflect less the imaging light. Second, the air plasma wrinkled more severely the surface of the smaller jets, generating a rough shock-reflecting surface that diffused the shock reflections, which in turn affected the wave interference that generates the shock train [16,24].

B. The amplitude and the decay of the shock wave pressure

The good visibility of shocks in the 30- and 70- μm jets allowed us to measure the pressure of the leading shock wave up to time delays of 225 ns, longer than the 0- to 40-ns delay range investigated before [16]. To determine the shock pressure, we first measured the shock velocity for each consecutive set of time delays, by differentiating the average shock positions with respect to the time. We then used the relation between shock velocity and pressure in water to determine the shock pressure, using the procedure described by Blaj *et al.* [16], for a water temperature of 22°C. Shock pressure measurements could be made for all high-visibility shocks, and for part of the low-visibility shocks (see Fig. 3).

The top shock pressures are shown in Fig. 4 as a function of the time delay, and data for the bottom shocks is available in the Supplemental Materials [25]. At the smallest time delays, the shock amplitude was on the order of 1 GPa and increased with pulse energy. It decayed by at least one order of magnitude in less than 100 ns, more rapidly in the thinner jets. These characteristics are similar to the properties of XFEL-induced shocks. A feature not observed previously is that in the 30- μm diameter jets, after ≈ 100 ns the shock pressure remained approximately constant at 40 MPa.

The shock trains in jets have been interpreted as a maximal intensity sound wave, whose amplitude is fundamentally limited by cavitation at the negative pressure peaks in the wave [16]. If the initial shock exceeds the amplitude of the maximal wave, then cavitation will dissipate the energy of the shock train, and the shock pressure will decay rapidly until the negative pressure swings are no longer large enough to induce cavitation. The approximately 40-MPa constant shock pressure observed at long time delays can be explained by this mechanism. (i) Assuming approximately symmetric pressure oscillations, the value of the constant pressure implies a cavitation pressure limit of ≈ -40 MPa; this is a plausible value for cavitation because it falls between the peak negative pressures achieved in water during ultrasonic [27] and optofluidic [5,28] cavitation studies. (ii) Ultrasonic attenuation, another mechanism that could lower the shock amplitude, is predicted to be negligible for our experimental conditions [16].

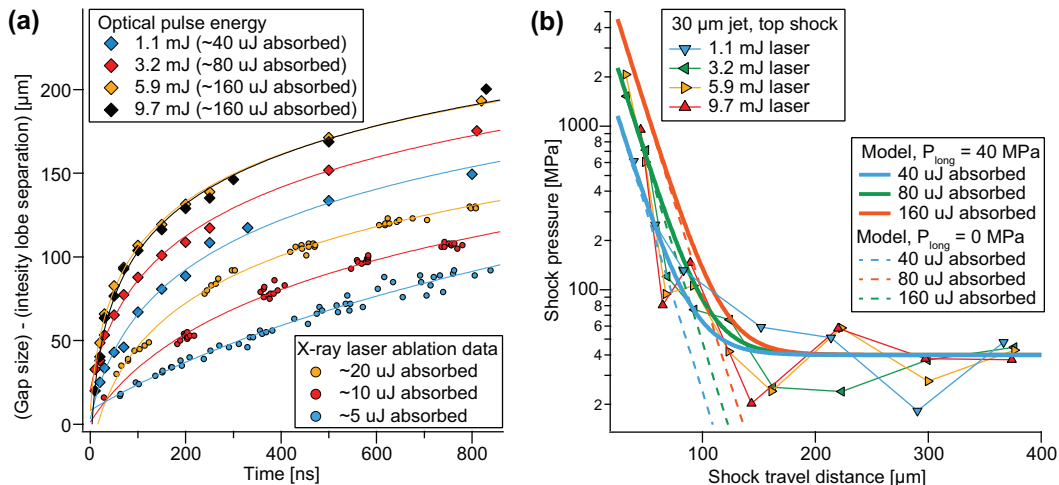


FIG. 5. (a) Comparison of the jet gaps produced by the green laser and an x-ray laser. The similar temporal dynamics allows the estimation of the energy deposited in the jet by the green laser, as listed in the caption. The continuous lines are logarithmic fits to the data. (b) Comparison of the shock pressures with models based on the decay of XFEL-induced shock pressures [see Eqs. (1) and (2)]. The data points are the same as the ones displayed in Fig. 4(a) and have the same error bars; the error bars in Fig. 5(b) are shown only for the 3.2-mJ data to avoid excessive clutter in the graph.

IV. DISCUSSION

A. Quantitative comparisons with x-ray laser ablation experiments

The size of the ablation gap and the amplitude of the shocks both depend on the amount of energy deposited in the jet. For x-ray laser ablation, the amount of deposited energy can be calculated precisely from the energy of the radiation pulse, and it is possible to predict the size of the gap analytically [4,18]. Similar predictions for optical ablation are challenging because in general it is not possible to calculate the energy deposited during optical ablation. Nevertheless, the energy deposited by the green laser into the jet can be estimated using the size of the gap, because at time delays that are long compared to the timescale of the laser pulse, the size of the gap was shown to obey a universal approximate analytical solution, independent of the method used to deposit energy [18]. According to this solution, for a given jet diameter and jet liquid, the gap size is a function of only the beam size and of the deposited energy. The size of the beams in our experiments and in XFEL studies was comparable and smaller than the jet diameter, which leaves the pulse energy as the dominant factor in determining the gap size. Therefore, if the dependence of the gap size on the deposited energy is known from XFEL experiments for a given jet liquid and jet diameter, the energy deposited by the green laser can be determined from the gap size.

The dynamics of the gap expansion in 30- μm diameter jets for all pulse energies is shown in Fig. 5(a) along with corresponding x-ray laser jet explosion data [16]. In our experiments, the energy absorption pattern had two maxima displaced vertically along the jet by 25–40 μm , depending on the pulse energy. In the 30- μm jets, the ablation plasma in the liquid sometimes spread across the whole jet laterally, and the jet explosions were relatively symmetric along the laser propagation direction. Given this symmetry, we regarded the ablation process as a double ablation by two separated light beams, with each beam driving its own gap and shock waves. If we neglect the interaction between the two explosions, then the experimental gap size is equal to the size of the gap made by a single beam plus the separation between beams. In Fig. 5(b) we subtracted the separation between hot spots from the observed gap size, therefore the data plotted in the figures corresponds to the gap sizes that would be generated by a single hot spot.

The growth of the optically driven gaps had the same qualitative dynamics as the XFEL-driven gaps [4], with a rate of growth that slowed down in time. This behavior was also observed in experiments with strongly absorbed soft x rays [26]. In principle, the gap data in Fig. 5(a) can be fit using the universal analytical solution for the gap growth [18] to determine the deposited energy, but the range of time delays was not sufficient for precise measurements. Instead, we estimated the deposited energy based on the observation that after the rapid growth phase, the size of the gap depends logarithmically on the deposited energy [4]. The vertical spacing between consecutively larger gaps in Fig. 5(a) is approximately constant at 800 ns and equal to the spacing of the XFEL data for deposited pulse energies increased by factors of 2 (5, 10, and 20 μJ). Extrapolating this trend, the energy deposited by the green laser ranged between $\approx 40 \mu\text{J}$ and $\approx 160 \mu\text{J}$, as shown in the graph. From 5.9 to 9.7 mJ, the energy deposited did not change, reflecting a saturation in the deposited energy. This saturation may be due to the air plasma reflecting or absorbing part of the incoming pulse before it arrives at the jet.

The deposited energies can be used to estimate the energy density of the water plasma. From images taken after the plasma formed but before any shock separated from it, we estimated that the initial size of the plasma along the jet axis increased with the pulse energy and ranged between 5 and 10 μm . For a cylindrically symmetric plasma spanning laterally across the jet, the initial size corresponds to a plasma energy density of $\sim 30 \text{ kJ/cm}^3$ for all pulse energies. This energy density is comparable to the plasma energy density of 33–40 kJ/cm^3 reported for 580 nm, 6-ns laser pulses [29].

The shock pressure can also be estimated using the deposited energy. Experiments on XFEL-induced shocks in water showed that the leading shock initially propagates as a cylindrical wave while decaying due to geometrical spreading [17], and after it is constrained by the jet boundary it generates additional trailing shocks while decaying at an exponential rate [16]. Using the estimated deposited energies, we first estimated the amplitude of the leading shock at 10 μm from the beam axis, before it reached the jet surface, by interpolating the dependence of shock pressures on the pulse energy from the x-ray laser measurements (see Fig. S5 in the Supplemental Materials of Ref. [16]). We then assumed an inversely linear decay of the shock pressure with the distance [17] up to a distance equal to the jet radius, R , of 15 μm . From this distance we calculated the leading shock pressure, $P(x)$, using the empirical exponential decay law proposed by Blaj *et al.* [16],

$$P(x) = P(R) \times 10^{-(x-R)/(3R)}, \quad (1)$$

where x is the shock distance from the beam axis.

The pressure predicted by Eq. (1) is shown as dashed lines in Fig. 5(b) along with the experimental data. This prediction agrees within a factor of ~ 2 with the measurements at short time delays, but underestimates the shock pressures for propagation distances exceeding 100 μm . To account for the long-lived shock pressure we calculated a modified shock pressure, $P^*(x)$, which includes the constant shock pressure, P_{long} , observed at long time delays:

$$P^*(x) = P_{\text{long}} + [P(R) - P_{\text{long}}] \times 10^{-(x-R)/(3R)}. \quad (2)$$

We estimated the predictive accuracy of Eq. (2) using the measurements in 30 μm diameter jets. For pressures much larger than P_{long} (time delays below 50 ns), the average ratio between measurements and predictions was 0.88 ± 0.39 across all measurements. For the smallest pressures (time delays above 100 ns) the main uncertainty was the value of the long-lived shock pressure, $P_{\text{long}} = 39 \pm 12 \text{ MPa}$, calculated as the mean and standard deviation of measured shock pressures at time delays above 100 ns. Therefore, for our experiments the model had $\approx 50\%$ accuracy at high pressures and $\approx 25\%$ accuracy at low pressures. The two types of uncertainties can be combined to calculate prediction bands, and an example is given in the Supplemental Materials [25].

V. CONCLUSION

The generation of shock wave trains in liquid jets is a more general and robust phenomenon than it could be inferred from the initial observation in experiments that used x-ray lasers [16]. Here, we generated the shock trains despite the more complicated energy absorption dynamics in the optical regime, despite using a multimode laser beam with multiple intensity peaks, and despite conducting the experiments at ambient conditions. Our findings make future studies of the shock trains much more accessible because mJ-class nanosecond green lasers are one of the most common type of pulsed lasers.

The dynamics of the ablation and of the shock trains were surprisingly similar to the ones observed when using x-ray lasers, and had roughly the same scaling with the absorbed energy as in the XFEL experiments, despite the very large difference in wavelengths and in the energy absorption mechanisms. This common scaling allowed us to predict the pressure of the leading shock during propagation. The shock trains we observed had fewer and less ordered fronts than in the x-ray laser experiments, but it is possible that longer trains can be produced using lasers that have a higher beam quality.

A new feature uncovered by our study is the approximately decay-free propagation of shocks after they reached a pressure of approximately 40 MPa, in 30- μ m diameter water jets. This long-lived shock pressure is a potential problem for XFEL experiments that use \approx 100- μ m diameter liquid jets, such as solution-phase x-ray scattering experiments [30], at megahertz repetition rate XFELs [31,32]. At the same time, the long-lived shock trains open the possibility of designing pump-probe experiments where the samples are first subjected to high-amplitude and high-frequency sound waves in a liquid, and then are probed using x rays. Finally, the ability to transmit the shocks inside the nozzles suggests that the shocks can also be coupled into microfluidic chips, enabling new types of acoustofluidic experiments [33] where samples can be subjected to sound waves with high amplitudes without exposing the microfluidic chip to high-energy laser pulses.

ACKNOWLEDGMENTS

We thank M. Vamesu for experimental assistance. The green laser experiments were supported by the “Nucleu” program, funded by the Romanian Ministry for Education and Research, Project No. 19 06 01 05 2020, and by the Extreme Light Infrastructure-Nuclear Physics (ELI-NP) Phase II, a project cofinanced by the Romanian Government and the European Union through the European Regional Development Fund and the Competitiveness Operational Programme (1/07.07.2016, COP, ID 1334). The x-ray laser ablation data was recorded at the Linac Coherent Light Source (LCLS), SLAC National Accelerator Laboratory. Use of the LCLS is supported by the U.S. Department of Energy, Office of Science, Office of Basic Energy Sciences under Contract No. DE-AC02-76SF00515.

-
- [1] A. L. Klein, W. Bouwuis, C. W. Visser, H. Lhuissier, C. Sun, J. H. Snoeijer, E. Villermaux, D. Lohse, and H. Gelderblom, Drop shaping by laser-pulse impact, *Phys. Rev. Applied* **3**, 044018 (2015).
 - [2] D. Kurilovich, A. L. Klein, F. Torretti, A. Lassise, R. Hoekstra, W. Ubachs, H. Gelderblom, and O. O. Versolato, Plasma propulsion of a metallic microdroplet and its deformation upon laser impact, *Phys. Rev. Applied* **6**, 014018 (2016).
 - [3] S. Y. Grigoryev, B. V. Lakatosh, M. S. Krivokorytov, V. V. Zhakhovsky, S. A. Dyachkov, D. K. Ilmitsky, K. P. Migdal, N. A. Inogamov, A. Y. Vinokhodov, V. O. Companets, Y. V. Sidelnikov, V. M. Krivtsun, K. N. Koshelev, and V. V. Medvedev, Expansion and fragmentation of a liquid-metal droplet by a short laser pulse, *Phys. Rev. Applied* **10**, 064009 (2018).
 - [4] C. A. Stan, D. Milathianaki, H. Laksmono, R. G. Sierra, T. A. McQueen, M. Messerschmidt, G. J. Williams, J. E. Koglin, T. J. Lane, M. J. Hayes, S. A. H. Guillet, M. N. Liang, A. L. Aquila, P. R. Willmott,

- J. S. Robinson, K. L. Gumerlock, S. Botha, K. Nass, I. Schlichting, R. L. Shoeman, H. A. Stone, and S. Boutet, Liquid explosions induced by x-ray laser pulses, *Nat. Phys.* **12**, 966 (2016).
- [5] K. Ando, A. Q. Liu, and C. D. Ohl, Homogeneous Nucleation in Water in Microfluidic Channels, *Phys. Rev. Lett.* **109**, 044501 (2012).
- [6] C. A. Stan, P. R. Willmott, H. A. Stone, J. E. Koglin, M. Liang, A. L. Aquila, J. S. Robinson, K. L. Gumerlock, G. Blaj, R. G. Sierra, S. Boutet, S. A. H. Guillet, R. H. Curtis, S. L. Vetter, H. Loos, J. L. Turner, and F. J. Decker, Negative pressures and spallation in water drops subjected to nanosecond shock waves, *J. Phys. Chem. Lett.* **7**, 2055 (2016).
- [7] D. Veyssset, U. Gutierrez-Hernandez, L. Dresselhaus-Cooper, F. De Colle, S. Kooi, K. A. Nelson, P. A. Quinto-Su, and T. Pezeril, Single-bubble and multibubble cavitation in water triggered by laser-driven focusing shock waves, *Phys. Rev. E* **97**, 053112 (2018).
- [8] T. Pezeril, G. Saini, D. Veyssset, S. Kooi, P. Fidkowski, R. Radovitzky, and K. A. Nelson, Direct Visualization of Laser-Driven Focusing Shock Waves, *Phys. Rev. Lett.* **106**, 214503 (2011).
- [9] I. Prencipe, J. Fuchs, S. Pascarelli, D. W. Schumacher, R. B. Stephens, N. B. Alexander, R. Briggs, M. Buescher, M. O. Cernaianu, A. Choukourov, M. De Marco, A. Erbe, J. Fassbender, G. Fiquet, P. Fitzsimmons, C. Gheorghiu, J. Hund, L. G. Huang, M. Harmand, N. J. Hartley, A. Irman, T. Kluge, Z. Konopkova, S. Kraft, D. Kraus, V. Leca, D. Margarone, J. Metzkes, K. Nagai, W. Nazarov, P. Lutoslawski, D. Papp, M. Passoni, A. Pelka, J. P. Perin, J. Schulz, M. Smid, C. Spindloe, S. Steinke, R. Torchio, C. Vass, T. Wiste, R. Zaffino, K. Zeil, T. Tschentscher, U. Schramm, and T. E. Cowan, Targets for high repetition rate laser facilities: needs, challenges and perspectives, *High Power Laser Sci. Eng.* **5**, e17 (2017).
- [10] K. M. George, J. T. Morrison, S. Feister, G. Ngirmang, J. R. Smith, A. J. Klim, J. Snyder, D. Austin, W. Erbsen, K. D. Frische, J. Nees, C. Orban, E. A. Chowdhury, and W. M. Roquemore, High-repetition-rate (\geq khz) targets and optics from liquid microjets for high-intensity laser-plasma interactions, *High Power Laser Sci. Eng.* **7**, e50 (2019).
- [11] C. N. Danson, C. Haefner, J. Bromage, T. Butcher, J. C. F. Chanteloup, E. A. Chowdhury, A. Galvanauskas, L. A. Gizzi, J. Hein, D. I. Hillier, N. W. Hopps, Y. Kato, E. A. Khazanov, R. Kodama, G. Korn, R. X. Li, Y. T. Li, J. Limpert, J. G. Ma, C. H. Nam, D. Neely, D. Papadopoulos, R. R. Penman, L. J. Qian, J. J. Rocca, A. A. Shaykin, C. W. Siders, C. Spindloe, S. Szatmari, R. M. G. M. Trines, J. Q. Zhu, P. Zhu, and J. D. Zuegel, Petawatt and exawatt class lasers worldwide, *High Power Laser Sci. Eng.* **7**, e54 (2019).
- [12] S. Gales, K. A. Tanaka, D. L. Balabanski, F. Negoita, D. Stutman, O. Tesileanu, C. A. Ur, D. Ursescu, I. Andrei, S. Ataman, M. O. Cernaianu, L. D'Alessi, I. Dancus, B. Diaconescu, N. Djourellov, D. Filipescu, P. Ghenuche, D. G. Ghita, C. Matei, K. Seto, M. Zeng, and N. V. Zamfir, The Extreme Light Infrastructure-Nuclear Physics (ELI-NP) facility: New horizons in physics with 10 PW ultra-intense lasers and 20 MeV brilliant gamma beams, *Rep. Prog. Phys.* **81**, 094301 (2018).
- [13] U. Weierstall, Liquid sample delivery techniques for serial femtosecond crystallography, *Philos. Trans. Roy. Soc. B Biol. Sci.* **369**, 20130337 (2014).
- [14] M. L. Gruenbein and G. N. Kovacs, Sample delivery for serial crystallography at free-electron lasers and synchrotrons, *Acta Crystallogr. D Struct. Biol.* **75**, 178 (2019).
- [15] J. D. Koralek, J. B. Kim, P. Bruza, C. B. Curry, Z. J. Chen, H. A. Bechtel, A. A. Cordones, P. Sperling, S. Toleikis, J. F. Kern, S. P. Moeller, S. H. Glenzer, and D. P. DePonte, Generation and characterization of ultrathin free-flowing liquid sheets, *Nat. Commun.* **9**, 1353 (2018).
- [16] G. Blaj, M. N. Liang, A. L. Aquila, P. R. Willmott, J. E. Koglin, R. G. Sierra, J. S. Robinson, S. Boutet, and C. A. Stan, Generation of high-intensity ultrasound through shock propagation in liquid jets, *Phys. Rev. Fluids* **4**, 043401 (2019).
- [17] C. A. Stan, K. Motomura, G. Blaj, Y. Kumagai, Y. W. Li, D. You, T. Ono, A. Kalita, T. Togashi, S. Owada, K. Tono, M. Yabashi, T. Katayama, and K. Ueda, The magnitude and waveform of shock waves induced by x-ray lasers in water, *Appl. Sci. Basel* **10**, 1497 (2020).
- [18] A. M. Gañán-Calvo, Scaling Laws of an Exploding Liquid Column Under an Intense Ultrashort X-ray Pulse, *Phys. Rev. Lett.* **123**, 064501 (2019).
- [19] T. Paula, S. Adami, and N. A. Adams, Analysis of the early stages of liquid-water-drop explosion by numerical simulation, *Phys. Rev. Fluids* **4**, 044003 (2019).

- [20] A. Charvat, B. Stasicki, and B. Abel, Product screening of fast reactions in IR-laser-heated liquid water filaments in a vacuum by mass spectrometry, *J. Phys. Chem. A* **110**, 3297 (2006).
- [21] V. Aleksandrov, G. Bleotu, L. Caratas, R. Dabu, I. Dancus, R. Fabbri, V. Iancu, B. Ispas, M. Kiss, A. Lachapelle, A. Lazar, M. Masruri, D. Matei, M. Merisanu, V. Mohanan, A. Naziru, D. Nistor, R. Secareanu, M. Talposi, A. Toader, A. Toma, and D. Ursescu, Upgrading design of a multi-TW femtosecond laser, *Rom. Rep. Phys.* **72**, 413 (2020).
- [22] A. Vogel and V. Venugopalan, Mechanisms of pulsed laser ablation of biological tissues, *Chem. Rev.* **103**, 577 (2003).
- [23] M. L. Gruenbein, J. Bielecki, A. Gorel, M. Stricker, R. Bean, M. Cammarata, K. Doerner, L. Fröhlich, L. Hartmann, S. Hauf, M. Hilpert, Y. Kim, M. Kloos, R. Letrun, M. Messerschmidt, G. Mills, G. Nass Kovacs, M. Ramilli, C. M. Roome, T. Sato, M. Scholz, M. Sliwa, J. Sztuk-Dambietz, M. Weik, B. Weinhausen, N. Al-Qudami, D. Boukhelef, S. Brockhauser, W. Ehsan, M. Emon, S. Esenov, H. Fangohr, A. Kaukher, T. Kluyver, M. Lederer, L. Maia, M. Manetti, T. Michelat, A. Münnich, F. Pallas, G. Palmer, G. Previtali, N. Raab, A. Silenzi, J. Szuba, S. Venkatesan, K. Wrona, Z. Zhu, R. B. Doak, R. L. Shoeman, L. Fouca, J.-P. Colletier, A. P. Mancuso, T. R. M. Barends, C. A. Stan, and I. Schlichting, Megahertz data collection from protein microcrystals at an x-ray free-electron laser, *Nat. Commun.* **9**, 3847 (2018).
- [24] L. F. Henderson, On the refraction of shock waves, *J. Fluid Mech.* **198**, 365 (1989).
- [25] See Supplemental Materials at <http://link.aps.org/supplemental/10.1103/PhysRevFluids.5.123402> for videos showing a selection of ablation images over a comprehensive range of conditions, and a pdf file containing additional shock pressure measurements, a detailed description of the pressure decay model and its comparison to bottom shock data, and a description of the videos including how they were assembled.
- [26] M. O. Wiedorn, S. Awel, A. J. Morgan, K. Ayyer, Y. Gevorkov, H. Fleckenstein, N. Roth, L. Adriano, R. Bean, K. R. Beyerlein, J. Chen, J. Coe, F. Francisco Cruz-Mazo, T. Ekeberg, R. Graceffa, M. Heymann, D. A. Horke, J. Knoška, V. Mariani, R. Nazari, D. Oberthür, A. K. Samanta, R. G. Sierra, C. A. Stan, O. Yefanov, D. Rompotis, J. Correa, B. Erk, R. Treusch, J. Schulz, B. G. Hogue, A. M. Gañán-Calvo, P. Fromme, J. Küpper, A. V. Rode, S. Bajt, R. A. Kirian, and H. N. Chapman, Rapid sample delivery for megahertz serial crystallography at x-ray FELs, *IUCrJ* **5**, 574 (2018).
- [27] Frederic Caupin and Eric Herbert, Cavitation in water: A review, *C. R. Phys.* **7**, 1000 (2006).
- [28] X. X. Lyu, S. C. Pan, X. Y. Hu, and N. A. Adams, Numerical investigation of homogeneous cavitation nucleation in a microchannel, *Phys. Rev. Fluids* **3**, 064303 (2018).
- [29] J. Noack and A. Vogel, Laser-induced plasma formation in water at nanosecond to femtosecond time scales: Calculation of thresholds, absorption coefficients, and energy density, *IEEE J. Quant. Electron.* **35**, 1156 (1999).
- [30] K. H. Kim, J. G. Kim, S. Nozawa, T. Sato, K. Y. Oang, T. Kim, H. Ki, J. Jo, S. Park, C. Song, T. Sato, K. Ogawa, T. Togashi, K. Tono, M. Yabashi, T. Ishikawa, J. Kim, R. Ryoo, J. Kim, H. Ihee, and S. Adachi, Direct observation of bond formation in solution with femtosecond x-ray scattering, *Nature* **518**, 385–389 (2015).
- [31] W. Decking, S. Abeghyan, P. Abramian, A. Abramsky, A. Aguirre, C. Albrecht, P. Alou, M. Altarelli, P. Altmann, K. Amyan, V. Anashin, E. Apostolov, K. Appel, D. Auguste, V. Ayvazyan, S. Baark, F. Babies, N. Baboi, P. Bak, V. Balandin, R. Baldinger, B. Baranasic, S. Barbanotti, O. Belikov, V. Belokurov, L. Belova, V. Belyakov, S. Berry, M. Bertucci, B. Beutner, A. Block, M. Blocher, T. Bockmann, C. Bohm, M. Bohnert, V. Bondar, E. Bondarchuk, M. Bonezzi, P. Borowiec, C. Bosch, U. Bosenberg, A. Bosotti, R. Bospflug, M. Bousonville, E. Boyd, Y. Bozhko, A. Brand, J. Branlard, S. Briechele, F. Brinker, S. Brinker, R. Brinkmann, S. Brockhauser, O. Brovko, H. Bruck, A. Brudgam, L. Butkowski, T. Buttner, J. Calero, E. Castro-Carballo, G. Cattalanotto, J. Charrier, J. Chen, A. Cherepenko, V. Cheskidov, M. Chiodini, A. Chong, S. Choroba, M. Chorowskils, D. Churanov, W. Cichalewski, M. Clausen, W. Clement, C. Cloue, J. A. Cobos, N. Coppola, S. Cunis, K. Czuba, M. Czwalinna, B. D’Almagne, J. Dammann, H. Danared, A. D. Wagner, A. Delfs, T. Delfs, F. Dietrich, T. Dietrich, M. Dohlus, M. Dommach, A. Donat, X. Dong, N. Doynikov, M. Dressel, M. Duda, P. Dudas, H. Eckoldt, W. Ehsan, J. Edam, F. Eints, C. Engling *et al.*,

- A MHz-repetition-rate hard x-ray free-electron laser driven by a superconducting linear accelerator, *Nat. Photon.* **14**, 391–397 (2020).
- [32] P. Abbamonte, F. Abild-Pedersen, P. Adams, M. Ahmed, F. Albert, R. Alonso-Mori, P. Anfinrud, A. Aquila, M. Armstrong, J. Arthur, J. Bargar, A. Barty, U. Bergmann, N. Berrah, G. Blaj, H. Bluhm, C. Bolme, C. Bostedt, S. Boutet, G. Brown, P. Bucksbaum, M. Cargnello, G. Carini, A. Cavalleri, V. Cherezov, W. Chiu, Y. Chuang, D. Cocco, R. Coffee, G. Collins, A. Cordones-Hahn, J. Cryan, G. Dakovski, M. Dantus, H. Demirci, P. Denes, T. Devereaux, Y. Ding, S. Doniach, R. Dörner, M. Dunne, H. Durr, T. Egami, D. Eisenberg, P. Emma, C. Fadley, R. Falcone, Y. Feng, P. Fischer, F. Fiuza, L. Fletcher, L. Foucar, M. Frank, J. Fraser, H. Frei, D. Fritz, P. Fromme, A. Fry, M. Fuchs, P. Fuoss, K. Gaffney, E. Gamboa, O. Gessner, S. Ghimire, A. Gleason, S. Glenzer, T. Gorkhover, A. Gray, M. Guehr, J. Guo, J. Hajdu, S. Hansen, P. Hart, M. Hashimoto, J. Hastings, D. Haxton, P. Heimann, T. Heinz, A. Hexemer, J. Hill, F. Himpel, P. Ho, B. Hogue, Z. Huang, M. Hunter, G. Hura, N. Huse, Z. Hussain, M. Ilchen, C. Jacobsen, C. Kenney, J. Kern, S. Kevan, J. Kim, H. Kim, P. Kirchmann, R. Kirian, S. Kivelson, C. Kliewer, J. Koralek *et al.*, New science opportunities enabled by LCLS-II x-ray lasers, Report SLAC-R-1053 (SLAC National Accelerator Laboratory, Menlo Park, CA, 2015).
- [33] J. Friend and L. Y. Yeo, Microscale acoustofluidics: Microfluidics driven via acoustics and ultrasonics, *Rev. Mod. Phys.* **83**, 647 (2011).